Journal of Materials Chemistry C

Accepted Manuscript

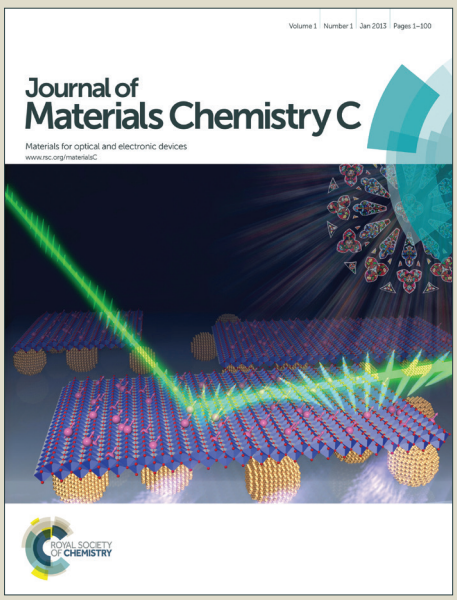

ROYAL SOCIETY OF CHEMISTRY

www.rsc.org/materialsC

Journal Name

RSCPublishing

ARTICLE

Computational Studies on Magnetism and Optical Properties of Transition Metal Embedded Graphitic Carbon Nitride Sheet

Dibyajyoti Ghosh[a], Ganga Periyasamy[b], Bradraj Pandey,[c] and Swapan K. Pati*[c]

Cite this: DOI: 10.1039/x0xx00000x

Received 00th January 2012,
Accepted 00th January 2012

DOI: 10.1039/x0xx00000x

www.rsc.org/

Using density functional theory (DFT), we have explored the structural, electronic, magnetic and optical properties of two-dimensional 3d-transition metal (TM) embedded graphitic carbon nitride (g-C_3N_4) sheet. g-C_3N_4 sheet structurally gets modified in different ways depending upon the radius of embedded TM atoms and crystal field stabilization energy gained by corresponding geometry. Bare g-C_3N_4 which is wide-gap semiconductor becomes metallic upon TM inclusion. The d-orbitals of TMs hybridize with p_π-orbitals of g-C_3N_4 framework and close the band gap in TM-embedded g-C_3N_4 (TM-g-C_3N_4). Interestingly, for V, Cr and Fe embedded g-C_3N_4, TM atoms interact ferromagnetically to each other and results a ferromagnetic ground state. However, Mn couples antiferromagnetically and Cu and Zn are nonmagnetic in the ground state of their corresponding TM-g-C_3N_4 sheets. Due to structural distortion, Co- and Ni-g-C_3N_4 do not have well-ordered magnetic orientation. Performing Heisenberg model based Monte Carlo simulations we predict that V-, Cr- and Fe-g-C_3N_4 possess Curie temperatures (T_c) 205 K, 170.5 K and 115 K, respectively. Furthermore, these modified g-C_3N_4 sheets also show the prominent absorption at low energy which evidently proves the efficient photoabsorption capacity of them. The present study demonstrates the multifunctional behaviour of TM-g-C_3N_4 where it shows a great promise of application for various fields such as memory devices, photocatalysis.

Introduction

At present, electronic memory related research is majorly directed to miniaturize the size of the device. [1-3] One promising way to shrink the size is to realize characteristics of bulk magnetic materials in nanoscale entities such as zero-dimensional (0D) molecules, [4-6] nanoclusters, [7, 8] one-dimensional (1D) organic polymers, [9, 10] organometallic sandwich complexes [11-13] , nanowires, [14, 15] two dimensional (2D) sheets[16-25] etc. Regular spin ordering in these magnetic materials is most essential to use them for memory and spintronics applications. [26-28] Even though intensive efforts are dedicated to search for such materials by both experimentalists as well as theoreticians, still success is limited. [29] In recent times, various 2D sheet structures have attracted a huge attention from scientific community because of their easy synthesis processes and various unusual properties. Numerous 2D sheet materials such as graphene[30, 31], hexagonal boron nitride (h-BN), [32, 33] molybdenum disulphide (MoS_2) [34, 35], magnesium oxide (MnO_2) [21, 36], carbon nitride graphene [37-40] have already been explored systematically. However, most of these materials do not possess any intrinsic spin polarization which makes them quite useless for above mentioned applications. Incorporation of spin-polarized first row TMs metal (i.e. V-Zn) atoms in these systems is an easy and widely studied way to induce spin moment in them. [20 , 41] However, previous studies have shown that as these TMs get adsorbed very weakly on top of regular graphene and h-BN sheets, they remain mobile in nature. [42, 43] To localize these TMs, several types of point defect (i.e. single or double vacancy) have been created in these 2D sheets. [41, 44-46] Real time dynamics of metal trapping on the defect sites of graphene has been probed using aberration-corrected transmission electron microscopy.[47] Following this way, one can get a sheet of metal-embedded material with controlled morphology and architecture with well-defined geometry, where the TM atoms can be uniformly and separately distributed without any cluster formation.[47] However, creating regular vacancies in graphene or h-BN sheet in a controlled way is always experimentally challenging task. In such a situation, one should search for some structurally stable 2D-sheet materials which can trap TM atoms strongly as well as in regular way. In the present study, we have

demonstrated one of the mono-layered graphitic carbon nitride, g-C_3N_4 as a 2D-sheet which can meet above requirements quite efficiently. g-C_3N_4 of our interest is heptazine-based which is most stable structure among all graphitic carbon nitrides (see Figure 1). [48] Several groups have already synthesized and characterized transition metal-doped g-C_3N_4 in bulk-layered form.[49-52] Nevertheless, recent reports of preparation of ultrathin g-C_3N_4 using liquid phase exfoliation process and trapping of TM atoms in mesoporous g-C_3N_4, strongly supports possibility of experimental realization of our model material where TM atoms are get trapped in the monolayer of g-C_3N_4 sheet. [53, 54]

g-C_3N_4 is a 2D-sheet like material which is stacked in third dimension via weak van der Waals forces. [48] It is a highly inexpensive and thermally stable wide-gap semiconductor. [48, 55-57] The ultrathin sheet of it is extensively used in various fields, such as optical sensing, hydrogen production, oxygen reduction, bioimaging etc. due to its unique photocatalytic and electronic properties. [50, 53, 54, 58] Moreover, it has been proved that removal of third dimension makes this material a better one than its bulk form in terms of visible-light photoresponse.[58, 59] A huge effort have also devoted to modify the intrinsic characteristics as well as finding new properties of layered g-C_3N_4 by doping it with various non-metals and metals such as P, S, Fe, V, Cu, Zn etc. [51, 52, 60, 61] Chen *et. al.* have confirmed that Fe containing g-C_3N_4 can catalyse the oxidation of benzene to phenol. [60] Wang *et. al.* synthesized Fe, Zn containing g-C_3N_4 which are more-efficient photocatalysts than that of bare g-C_3N_4. [51] However, up to our knowledge, the effects of inclusion of metals (mostly 3d transition metals) in monolayer of g-C_3N_4 and their possible application in electronics and optics have not been explored computationally. In present work, the structural, electronic, magnetic and optical properties of these TM-g-C_3N_4 where TM = V to Zn have been explored in details using density functional theory (DFT). We found that structural modification of these sheets is sensitive towards ionic radius and crystal field splitting of embedded TM. The electronic and magnetic properties of sheets also get hugely modified upon TM inclusion. Interestingly, V-, Cr- and Fe-g-C_3N_4 have ferromagnetically ordered states which are quite stable up to 205 K, 170.5 K and 115 K. Moreover, metal embedded sheets show prominent absorption at visible light energy range.

Computational Details

We have used spin-polarized density functional theory (DFT) as implemented in Vienna ab initio simulation package (VASP). [62] For exchange-correlation, we have used Perdew-Burke-Ernzerhof (PBE) functional within the Generalized Gradient Approximation (GGA). [63] As it is well known that partially filled d-orbital containing systems can't be described accurately by using only GGA functional, we have used GGA+U method. [64] In this method, s and p-orbitals are described by only GGA functional, whereas localized d-orbitals are taken care with Coulomb and exchange corrections. Following several other studies of these 3d-transition metal containing organometallic complexes, we have considered correlation energy (U) as 4 eV and exchange energy (J) as 1 eV for our investigation.[20, 65, 66] We have used projected augmented wave (PAW) method[67, 68] with a plane-wave basis set having cut-off energy of 400 eV for all systems. To interpolate the correlation energy, we have performed Vosko-Wilk-Nusir modification for spin polarized calculations. [69] For these two-dimensional sheets, a vacuum of 15 Å has been used to avoid spurious interaction in non-periodic directions (i.e. z direction here). To find magnetic ground state of these systems, we have taken a (2×2) supercell. For periodic calculations, we have used Monkhorst-Pack of 7×7×1 and 5×5×1 k-point grid (total number of k-points is 25 and 13, respectively) to sample the 2D Brillouin zone of unit cell and (2×2) supercell of TM-g-C_3N_4, respectively. For geometry optimizations, we have not imposed any symmetry constrains and inter-atomic forces are relaxed up to 0.01 eV/Å. To ensure the structural stabilization of these sheets under finite temperature, we have done spin polarized *ab-initio* molecular dynamics (AIMD) simulations taking a 2×2 supercell. We have varied the temperatures (T) and carried out the simulations at three different temperatures, namely T = 300 K, T = 500 K and T = 1000 K. We keep these temperatures fixed using Nose-Hoover thermostat.[70, 71] To study magnetic ordering at finite temperature, Heisenberg model based Monte Carlo (MC) simulation is performed by taking a supercell of 80×80 sites and involving 2×10^6 MC steps. For optical property calculation, we have calculated the frequency-dependent dielectric matrix using GGA functional and k-mesh of 13×13×1 to sample the Brillouin zone finely. The imaginary part of this dielectric matrix is used to calculate desired absorption spectra.[69] To know about the structural stability of these structures, the binding energy have been calculated using following formula, [72]

$$E_{bind} = E_{sheet} + E_{TM} - E_{sheet\text{-}TM,}$$

where E_{sheet} and E_{TM} are the energy of bare g-C_3N_4 and chemical potential of TM atom in its bulk phase, respectively. $E_{sheet\text{-}TM}$ denotes the total energy of g-C_3N_4 with TM atoms embedded within it.

Results and Discussion

First, metal-free buckled single-layered g-C_3N_4 sheets are explored very briefly to understand its general geometric and electronic properties. The unit cell of this sheet has been constructed by tri-s-triazine (i.e. heptazine) where three triazine rings get fused and forms triangular core group (see Figure 1a). Three of these heptazine units are connected through tertiary amino group. The unit cell contains three types of N atoms named as N_{edge}, N_{bridge} and N_{inner} and two types of C atoms (i.e. C_{bridge} and C_{inner}) as shown in Figure 1a. The N_{edge} atoms are at the edge of the cavity and are 2-fold coordinated with two C atoms, whereas N_{bridge} and N_{inner} which are 3-fold coordinated with C atoms, links three heptazine units and remain at the middle of heptazine unit, respectively. Both types of C atom are tri-coordinated with N, two of which are N_{edge}. C_{bridge} atoms are coordinated with N_{bridge} atoms, whereas C_{inner} is connected to

N_{inner}. The ground state structure shows prominent buckling nature for this 2D-sheet which is consistent with previous experimental and theoretical reports (Figure 1b and 1c). [55, 56] Moreover, we found out that planar monolayer g-C_3N_4 is higher in energy by 0.042 eV/atom than the buckled one. The optimized distance between two nitride pores is 6.9 Å which is also consistent with the experimental observation (6.81 Å). [56] These results validate our computational methods for further investigation. The cavity is surrounded by six lone pair containing electron rich nitrogen (N_{edge}) and three tri-coordinated nitrogen (N_{bridge}), (see Figure 1b). From charge

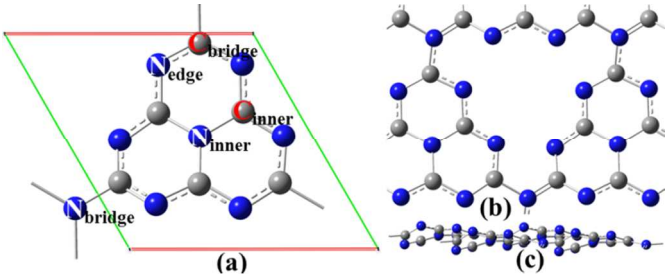

Figure 1. Atomic configuration of bare sheet of g-C_3N_4; (a) unit cell, (b) zoomed top view of electron rich cavity where TM atoms get trapped and (c) side view of g-C_3N_4 sheet. Blue and grey balls are nitrogen and carbon atoms, respectively.

density distribution plot, (see Figure S1) it is evident that these N atoms all together make the cavity environment highly electron rich in nature because of which it is rightly called as "nitrogen pots". [51] As a result, this cavity becomes ideal site for inclusion of positively charged transition metals ions. Using HSE06 functional [73], the pure g-C_3N_4 nanosheet appears as non-magnetic semiconductor with a band gap of 2.7 eV (see Figure S2 for PDOS of g-C_3N_4 nanosheet) which restricts this sheet to be used as efficient visible light photocatalyst. As mentioned previously, in the following part we will explore the structural, electronic, magnetic and optical properties of 3d-TM (V ($3d^34s^2$) to Zn ($3d^{10}4s^2$)) atom embedded g-C_3N_4 sheets. Note that, for present study, we considered structures where single 3d TM atom gets embedded per N-cavity and form regularly separated TM decorated 2D porous sheets. We have also considered the possibility of trapping of TM atoms as dimers to investigate about their clustering tendency.

Structures

Metal embedded g-C_3N_4 sheets are optimized by considering a super-cell with four nitride cavities (i.e. 2×2 supercell) as shown in Figure S3. To start with, we have explored the structure of TM-g-C_3N_4. Generally, TM atoms have strong tendency to segregate on the surface of low-dimensional materials, where TM binding with surface is much weaker than in bulk phase. [74] From Table 1, it can be seen that for V, Cr, Mn and Fe embedded sheets, the binding energy is positive i.e. the TM atoms are more stable in the cavity of g-C_3N_4 system than that of their bulk phase. However, negative binding energies for Co, Ni, Cu and Zn imply that these TM atoms have tendency to segregate and form metal cluster in the cavity.

However, as pointed out by several groups,[75, 76] the possibility of dimer formation or aggregation should be confirmed by comparing the single atom and dimer binding energy with surface. Note that, cluster formation can be circumvented if TM dimer binding on that surface become less stable compared to single atom binding. Thus, we have calculated the clustering energy ($E_{cluster}$) which is defined as difference between binding energy of dimer ($E_{b,di}$) and single ($E_{b,mono}$) TM in the g-C_3N_4 cavity,

$$E_{cluster} = E_{b,di} - E_{b,mono}$$

where both $E_{b,di}$, $E_{b,mono}$ are in eV/TM. Positive (negative) value of $E_{cluster}$ signifies that TM atoms are prone towards cluster formation (dispersion). From Table 1, it is evident that all TM atoms have negative clustering energy on this sheet. Thus, we can conclude that single TM atoms embedded g-C_3N_4 sheets under study are reasonably stable and prevent the segregation of TMs on the cavity. This is in full agreement with the experimental observations also.[49 50]

In these materials, because of strong hybridization between TM and host sheet, 4s levels are pushed well above the Fermi level. As a result, the effective electronic configuration of TM becomes $3d^{3\text{-}10}4s^0$ and these remain as cation with +2 charges (apart from Cu). Interestingly, the planarity of optimized TM-embedded g-C_3N_4 sheets increases with the decrease in TM's atomic number. Here, the TM atoms form strong chemical bonds with the nitrogen atoms in the cavity (N_{edge}) of the g-C_3N_4 host. However, the number of N_{edge} atoms involved in symmetric coordination with TM atoms varies as can be seen in Figure 2 and Table S1. In detail, V, Cr, Mn and Fe (considered as early transition metals) are almost symmetrically placed in the g-C_3N_4 cavity, whereas, Co, Ni, Cu and Zn (i.e. late transition metals) form asymmetric coordination in the g-C_3N_4 cavity (see Table S1). There are several factors which are responsible for having this trend in TM-g-C_3N_4 structures:

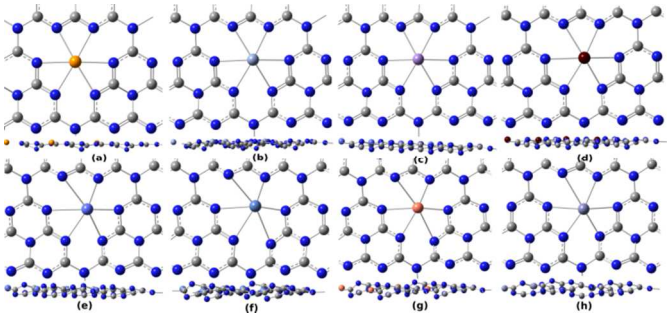

Figure 2. Top view and side view of TM-embedded g-C_3N_4 where TM is (a) V- (b) Cr- (c) Mn (d) Fe (e) Co (f) Ni (g) Cu and (h) Zn.

(1) Most importantly, size of cationic TM atoms. The crystal ionic radius of TM^{+2} are listed in the Table S2. [77] It is evident from the table that ionic radius for early TMs (i.e. V^{+2} to Fe^{+2}) are larger than that of late TMs (i.e. Co^{+2}, Ni^{+2}, Cu^{+1} and Zn^{+2}). To accommodate these larger early TM ions, flexible g-C_3N_4 sheet gets structurally modified. The TM embedded 2D-sheet

becomes almost planar where these metal ions sit at the centre of cavity and interact with all N_{edge} atoms almost symmetrically. The N_{inner} atom of heptazine unit moves out of the plane by ~0.7 Å to reduce the strain which gets generated as this unit become planar after coordinating to TM ions through N_{edge} atoms. As can be seen from Figure 2 and Table S1, V^{+2} and Fe^{+2} ions form a perfect hexagonal coordination with N_{edge} atoms whereas other early TM^{+2} (i.e. Cr^{+2} and Mn^{+2}) remain in little distorted hexagonal coordination environment. However, decrease in cationic metal atom size increases the possibility of insertion of TM atoms within cavity without major modification in bare buckled g-C_3N_4 sheets. As a result, cationic Co, Ni, Cu and Zn atoms get accommodated inside the non-planar cavity by forming strong covalent bonds with one/two N_{edge} atoms (see Table S1).

(2) The crystal field stabilization energy (CFSE) gained by V^{+2} and Fe^{+2} ions in hexagonal coordination is the reason behind the formation of perfect planar cavity for V-g-C_3N_4 and Fe-g-C_3N_4 sheet. Hexagonally coordinated crystal-field environment splits the d-bands of TM into four bands; doubly degenerate d_{xz} and d_{yz} (i.e. d_π bands) and non-degenerate d_z^2, $d_{x^2-y^2}$ and d_{xy} band (see Figure 3a). Quite obviously, three d-bands which are not in xy-plane become much stabilized than other two d-bands i.e. $d_{x^2-y^2}$ and d_{xy} which are in xy-plane and face the 2p orbitals of N_{edge} directly. Now, for V^{+2}, three d-electrons singly fill up these lowest three bands and gains huge stabilization energy in perfect hexagonal coordination. For Fe^{+2} ion, situation is bit different; there 6 d-electrons first fill-up all five majority spin bands singly and then sixth electron fills the minority band of d_z^2. As a result, here also system gains CFSE by remaining in perfect hexagonal coordination. On the other hand, for other early TM atoms CFSE gets reduced as the higher energetic d-bands i.e. $d_{x^2-y^2}$ and d_{xy} also get singly filled up by d-electrons. To circumvent this situation, these TMs remain in little distorted hexagonal coordination where $d_{x^2-y^2}$ and d_{xy} bands do not interact with 2p orbitals of N_{edge} that strongly as it is for perfect coordination. As a result, for these systems $d_{x^2-y^2}$ and d_{xy} bands remain near to the Fermi level and get filled up singly without losing much CFSE.

The optimized structures of these sheets can be seen the Figure 2 and important bond distances and bond angles are tabulated in Table S1. However, we find that the TM inclusion does not change the sheet structures drastically which is consistent with X-ray diffraction study of TM-g-C_3N_4. [51] To give a quantitative measurement about the buckling trend, we have calculated the extra energy for the unit cell of these complexes needed to form planar and symmetric cavities. These energies are denoted as destabilization energy ($E_{disstab}$ = $E_{planarTM\text{-}g\text{-}C3N4} - E_{optimized}$) and can be seen in Table 1. It can evidently be seen that the destabilization energy for buckled structures gets increased as one move from earlier to late TM atoms.

Further, to provide the evidence for stability of these TM-embedded g-C_3N_4 sheets under room temperature (i.e. 300 K), we have performed ab-initio molecular dynamics (AIMD) study. We have taken two structures, V-g-C_3N_4 and Cu-g-C_3N_4 for the investigation. After simulating for 5 picoseconds, it is evident that both sheets are quite stable in room temperature (see Figure S4). Like DFT calculated structures, V-g-C_3N_4 remains almost planar whereas Cu-g-C_3N_4 faces distortion after equilibration. To investigate the stability of these sheets at higher temperatures, we have performed AIMD study for 4 picoseconds at 500K and 1000K taking V-g-C_3N_4 as representative sheet. Figure S5 clearly illustrates that even at higher temperatures, the TM atoms remain in cavity without forming any kind of phase segregation. Thus, singly dispersed TM atoms on g-C_3N_4 are quite stable and avoid cluster formation as found in DFT calculation also. Note that, it is possible that phase segregation may occur at much higher time scale. However, within our short time scale MD simulations data, we provide evidence for the stability of these 2D-sheets. Importantly, rippling of 2D-sheet materials at finite temperature [78] is very prominent for these sheets and it increases as the temperature increases.

Table 1. Destabilization energy per unit cell of TM-g-C_3N_4, binding energies per unit cell, clustering energy per unit cell, magnetic moment per TM, total magnetic moment and exchange energies for per 2×2 supercell are tabulated.

Metal	V	Cr	Mn	Fe	Co	Ni	Cu	Zn
Destabilization energy (eV)	-	0.08	0.03	-	0.18	0.42	0.34	0.35
Binding Energy(eV)	1.87	3.65	4.48	0.68	-1.4	-1.97	-2.1	-1.4
Clustering Energy(eV)	-1.98	-1.03	-1.1	-1.15	-0.73	-0.60	-0.67	-0.78
Magnetic moment per TM	3	4	5	4	2	1	0	0
Magnetic moment per 2×2 supercell	12	16	20	16	-	-	0	0
ΔE_{ex} (meV)	-90	-80	20	-53	-	-	0	0

Electronic and Magnetic Properties

As mentioned earlier, bare g-C_3N_4 is wide-gap semiconductor where the valance and conduction bands are majorly localized at N_{edge} (majorly p_x and p_y orbitals) and N_{inner}/C (majorly p_z orbitals) atoms, respectively (see Figure S2). The inclusion of TM atoms in the cavity largely modifies the electronic[51] and magnetic properties of this sheet.

To begin with, we first explore the magnetism in these sheets. By plotting the spin density of early transition metal (V–Fe) embedded sheets we find that though most magnetic moments are localized at the metal atom, N_{edge} atoms also carry some small but finite moment (see Figure 3c for V-g-C_3N_4). Therefore, we focus on the nature of magnetic coupling between two neighbouring TM metal atoms as well as among the d-orbitals of TM and the p-orbitals of N_{edge} of g-C_3N_4. A 2×2 supercell has been considered for all 2D-sheets to determine the properties (see Figure S3). These supercells have also been optimized considering neighbouring Fe atoms coupled ferromagnetically (FM) as well as antiferromagnetically (AFM). The energies of these differently coupled systems are computed to calculate the exchange energy

(E_{ex}= E_{FM} − E_{AFM}). Corresponding spin densities of these two magnetic states of V-g-C_3N_4 can be seen in Figure S6. The E_{ex}, magnetic moment per TM atoms and magnetic moment per supercell have been tabulated in Table 1. Calculations show that V, Cr and Fe atoms are coupled ferromagnetically with each other, while Mn atoms exhibit an antiferromagnetic Mn–Mn coupling. Moreover, spin density plots show that neighbouring N_{edge} atoms are oppositely spin polarized with respect to corresponding early TMs (see Figure 3c and S6). This is consistent with studies of other TM-based organometallic 2D-sheets.[20] Sheets with Cu and Zn, have non-magnetic ground states as TMs are $3d^{10}$ systems here, containing all paired d-electrons. For Co- and Ni-g-C_3N_4, although locally each TM contains magnetic moments, we have not explored long range magnetic order of these sheets, because they are highly non-planar and imperfect for device applications.

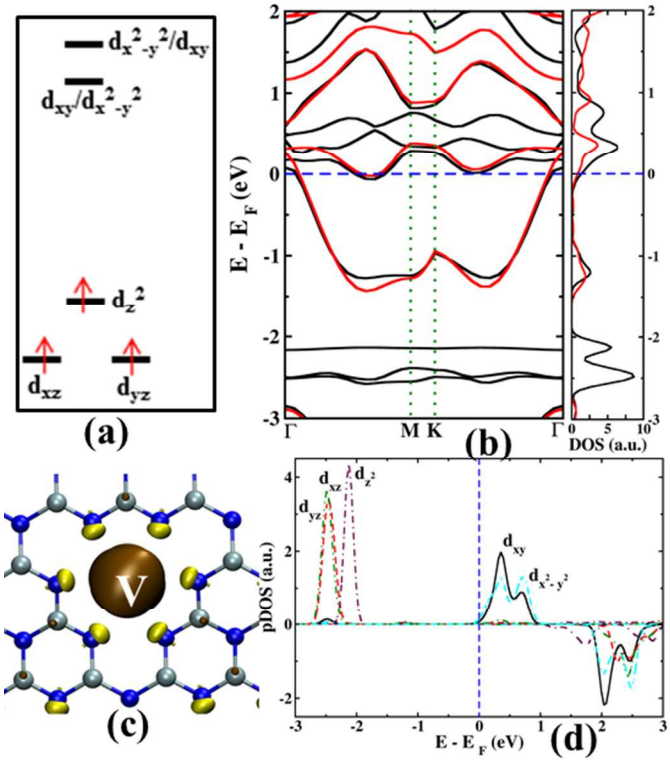

Figure 3. (a) The crystal field splitting of V in hexagonal environment (energy is not scaled); (b) band structure and corresponding DOS (Γ(0,0,0), M(1/2,1/2,0), K(2/3,1/3,0) are high symmetry K-points; symbols: black and red solid line denote majority and minority spin bands and blue dotted show Fermi levels); (c) Spin density with an isosurface of 0.025 e/Å^3 where up and down spin densities are represented as ochre and yellow coloured surfaces, respectively and (d) pDOS of d-orbitals on the V atom of FM V-g-C_3N_4 (symbols: solid black, dashed red, dashed doted maroon, dashed double doted deep green and double dashed doted cyan represent d_{xy}, d_{yz}, d_{z^2}, d_{xz} and $d_{x^2-y^2}$ orbitals, respectively).

Quite interestingly, our study predicts that sheets embedded with V, Cr and Fe atoms are having quite high ferromagnetic exchange energies i.e. -90, -80 and -53 meV, respectively (see Table 1). The large ferromagnetic exchange energies make these materials quite promising candidates for realizing moderate temperature 2D ferromagnetic sheet. We have explored this point further in latter part.

The origin of different kind of magnetic couplings in these planar sheets can be understood by considering spatial arrangement of interacting magnetic orbitals.[79, 80] According to the model proposed by Heitler and London, [79] the exchange coupling constant can be formulated as $J = K + 2\beta S_{overlap}$, where K denotes two-electron exchange integral term, β gives the resonance coupling and $S_{overlap}$ is the overlap integral of intervening orbitals. The definition of K and β suggest that K is negative and β is positive in sign. Therefore, we can express J as sum of J_{FM} and J_{AFM} ($J = J_{FM} + J_{AFM}$). Now, if the magnetically interacting orbitals are orthogonal to each other, $S_{overlap}$ and therefore antiferromagnetic term (i.e. J_{AFM}) become zero, resulting in only ferromagnetic coupling. For present study, as TM-TM distances are quite large in these sheets (see Table S1), the exchange interaction between them occurs via N_{edge} atoms of triazine unit. Thus, the spatial arrangement of interacting orbitals of TM and N_{edge} become very important in this context. Careful analysis show that near the Fermi energy of V-g-C_3N_4 and Fe-g-C_3N_4, p_z orbital of N_{edge} and almost empty majority spin band of V's $d_{xy}/d_{x^2-y^2}$ and minority spin band of same d-orbital of Fe, are present and majorly participate in exchange coupling. As these two orbitals (i.e. $d_{xy}/d_{x^2-y^2}$ and p_z) are orthogonal to each other, the FM coupling dominates for these two sheets. Situation is very similar for Cr-g-C_3N_4 where partially filled $d_{xy}/d_{x^2-y^2}$ orbitals of Cr interact orthogonally with p_z of N_{edge} and gives rise to strong ferromagnetic coupling among TM atoms. On the other hand, for Mn-g-C_3N_4, the interacting d-orbital is empty d_{z^2}, which is parallel to p_z orbital of N_{edge} and gives a finite $S_{overlap}$ value. As a result, both J_{FM} and J_{AFM} terms are non-zero for this system and AFM coupling dominates.

Furthermore, in order to investigate the electronic properties of TM-embedded 2D-sheet materials, we have analysed the band structures and density of states (DOS) of all the systems. Moreover, to understand the crystal field splitting of d-orbitals and local magnetic moment of TMs, we carefully have studied the projected DOS (pDOS) relevant to TM orbitals (see Figure 3d and 4). For 2D planar V-g-C_3N_4 framework, spin polarized band and DOS analysis evidently show the metallic nature of this sheet (Figure 3b). Moreover, exploring the band structure and pDOS of d-orbitals of V (Figure 3b, d), we find that spin splitting occurs for all the d-bands under perfect hexagonal crystal field (Figure 3a). The majority spin bands comprising of TM's d_{zx}, d_{yz} and d_{z^2} orbital remain as highly localized non-bonded states and stay far below the Fermi level, resulting in single occupancy in these bands. On the other hand, the p_z (i.e. p_π) orbitals of N_{inner}/C i.e. conduction band of pure g-C_3N_4 hybridize with stable d_{xz} and d_{yz} orbitals of V and produce highly dispersive almost spin-degenerated bands which cross the Fermi level near the Γ-point. Other two d-orbitals i.e. d_{xy} and $d_{x^2-y^2}$ mix themselves and are hybridized with spin-degenerate p_z orbitals of N_{edge}/C atoms. As mentioned previously, these d-orbitals are perpendicular to p_z orbitals and they do not interact with each other much. Thus, the bands

appear as less dispersive in nature. These are mostly unoccupied but also touch the Fermi level slightly (see Figure 3(b)). As a result, the V-g-C_3N_4 sheet shows a magnetic ground state with a total magnetic moment of 3μ_B/unit cell, where this moment is concentrated at the three low-lying nonbonded singly occupied d-orbitals, as can be seen in Figure 3d.

For Cr- and Mn-g-C_3N_4, the TMs remain in slightly distorted hexagonal crystal field environment. As a result, in these cases d-orbital splitting is not as prominent as it is for d-orbitals of V in V-g-C_3N_4. However, d-bands of these TM atoms split in the same manner as it is for V atom i.e. 2 (d_{xz}, d_{yz}) + 1 (d_z^2) + 1 (d_{xy}/$d_{x^2-y^2}$) + 1 ($d_{x^2-y^2}$/d_{xy}). Due to increase of d-electrons for Cr and Mn atoms (i.e. 4 and 5 electrons), higher lying majority spin bands which are from d_{xy} and $d_{x^2-y^2}$ orbitals

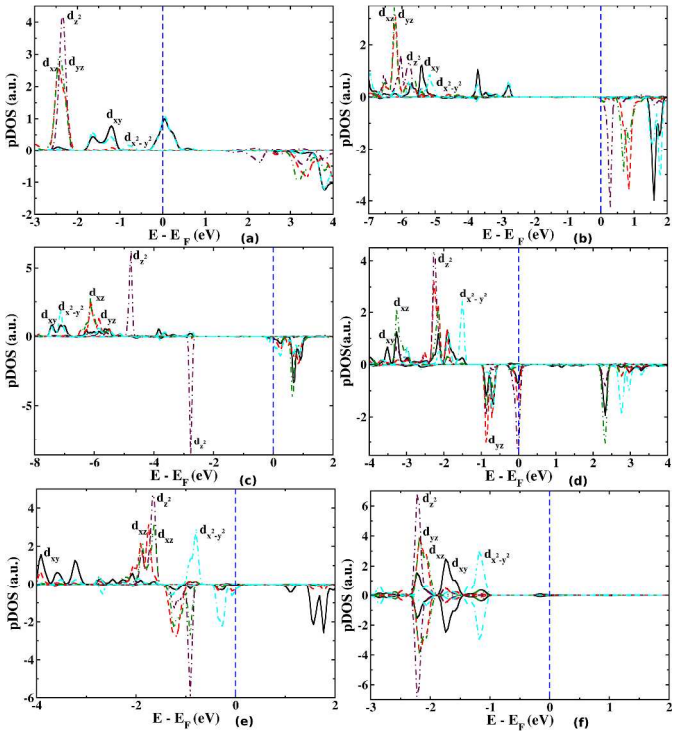

Figure 4. Projected DOS of d-orbitals on the TM atoms of TM-g-C_3N_4 where TM is (a) Cr, (b) Mn, (c) Fe, (d) Co, (e) Ni and (f) Cu.

also get singly occupied (Figure 4a,b). So, local magnetic moments of Cr and Mn in unit cell of them appear as 4 and 5 μ_B, respectively. For Fe-g-C_3N_4 as mentioned earlier, it has planar geometry and also after singly occupying all five majority d-bands (which is the case for Mn), sixth d-electron fills up the minority band of d_z^2 orbital giving rise to a magnetic moment of 4 μ_B/unit cell (Figure 4c). Analysing the band structures, plotted in Figure S7, it is prominent that all these 2D-sheets are metallic in nature as the conduction band of g-C_3N_4 becomes dispersive, interacting with d-orbitals and staying close to the Fermi level. At this point, one should note that, all early TM atoms remain in their corresponding high-spin states i.e. the spin pairing at low lying d-bands cause higher energy than the single occupancy at higher energy d-orbitals.

As the late transition metal atoms (i.e. Co, Ni, Cu and Zn) remain in highly distorted coordination environment, it becomes very complicated to determine what type of d-band splitting occurs for these metal atoms (Figure 4d,e,f). Nevertheless, the d-orbitals get strongly hybridized with the p-bands of g-C_3N_4 sheet and all majority spin bands of these TM metal atoms are occupied. For Co-g-C_3N_4, all minority spin bands are partially occupied and have collectively three electrons in them, giving a local magnetic moment of ~ 2μ_B/unit cell. In the same way, Ni-g-C_3N_4 possesses a magnetic ground state with a local magnetic moment of ~ 1μ_B/unit cell. As mentioned, Cu- and Zn-g-C_3N_4 show non-magnetic behaviour in their electronic ground state. Unlike other TM atoms, Cu remains in +1 oxidation state in Cu-g-C_3N_4 due to back donation of electrons from ligand to metal. Complete filling of d-orbitals i.e. d^{10} also gives extra stabilization to +1 oxidation state of Cu. Therefore, all the d-bands are completely filled up for Cu- and Zn-g-C_3N_4 and do not contain any unpaired electrons. Band structure calculations certainly show the metallic character for these sheets (see Figure S7).

As pointed out by several studies,[81, 82] during GGA+U based calculations, structural, electronic and magnetic properties of TM embedded nanostructures depend substantially on choice of U and J parameters. To investigate the influence of U and J on these properties of TM-g-C_3N_4, we have varied the effective U (i.e. U_{eff} = U − J) in the range 2–5 eV for all systems. We observed only little impact of U_{eff} parameter on the structural and magnetic properties of these 2D-sheets. We have given the results by considering Fe-g-C_3N_4 as an example. The insignificant changes in structural parameters (bond lengths and dihedrals of Fe-g-C_3N_4) with respect to various U_{eff} are apparent from Table S3. In the same way, the contribution of U_{eff} towards magnetic stability of these sheets has also been calculated by considering 2×1 supercell. We have plotted the total energy of two magnetic states (i.e. FM and AFM) verses U_{eff} for Fe-g-C_3N_4 in Figure S8. We find that the nature of the magnetic ground state (i.e. FM state) remains unchanged the range of U_{eff} value that is considered. The above mentioned results validate our choice of U and J parameters.

To use these ferromagnetic sheets in various applications, one needs to know their magnetic behaviour under finite temperature. Monte Carlo (MC) simulations using Ising model have been performed widely to estimate Curie Temperature (T_C). [20, 21, 37] For present study, we have carried out MC simulations considering complete Heisenberg Hamiltonian. The Hamiltonian can be expressed as follows, [83]

$$H = \sum_{<ij>} J_{ij}(S_{ix}S_{jx} + S_{iy}S_{jy} + S_{iz}S_{jz})$$

where *i*, *j* and J_{ij} are nearest neighbour magnetic sites and exchange coupling constant between them, respectively. S_{ix}, S_{iy}

and S_{iz} are x, y and z components of total spin (S_{tot}) at i^{th} magnetic centre of the 2D-sheet. To use this Hamiltonian for MC simulations, we need to know the *J* values (both its magnitude and sign). Detail calculation to estimate *J* can be found in Supporting Information. Here, we have taken V, Cr and Fe embedded sheets under consideration as these three sheets show higher E_{ex} values. The estimated *J* values from our calculations turn out to be -4.3meV, -2.22 meV and -1.5meV for V-, Cr- and Fe-g-C_3N_4, respectively. By plotting average of S_z per unit cell vs. temperature, it is evident that all three sheets retain their ferromagnetic spin ordering at low temperatures. The T_C values appear at the temperature of 205 K, 170.54 K and 115 K for V-, Cr- and Fe-g-C_3N_4, respectively (see Figure 5 and Figure S9). The values of T_C for V- and Cr-g-C_3N_4 are quite higher than the recently reported T_C of several 2D-sheets. [20, 21] Moderately higher T_C values of these sheets strongly indicate the potential usage of them in various advance magnetic device applications.

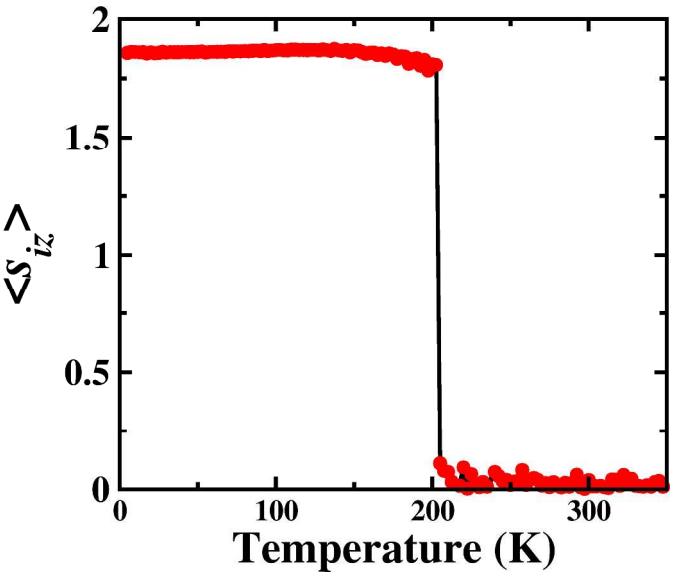

Figure 5. Values of average of Sz per unit cell of V-g-C_3N_4 with respect to the temperature. The transition from ferromagnetic to paramagnetic state occurs (i.e. Curie temperature) at 205K.

Optical Properties

As we discussed previously, pure g-C_3N_4 which is a wide-band semiconductor, has poor photoabsorption efficiency due to its inability to capture visible light. However, the inclusion of transition metals closes the band-gap of it and gives us a hint about the improvement in performance of absorbing visible light. [51] To confirm this point, we have plotted the absorption spectra of these sheet materials in the visible light energy range by calculating the imaginary part of dielectric function (see Figure 6). Analysing these spectra, one can clearly see that these materials can absorb low-energy light (i.e. < 3.3 eV) quite efficiently. For early TM (i.e. V–Fe) embedded g-C_3N_4, there are two major types of transition (1) p_π of C/N→ $d_{xy}/d_{x^2-y^2}$ of TM which gives low energy absorption peaks (i.e. < 2 eV; denoted as red '*' at Figure 6) and (2) d_{zx}/d_{yz} /d_{z^2} of TM → $d_{xy}/d_{x^2-y^2}$ of TM (i.e. d–d transition) which is responsible for absorption peaks at energy range of 2–3.5 eV (black '*' at Figure 6). For Co- and Ni-g-C_3N_4, all the transitions at 0–2 eV window appear because of the excitation of electrons from different d orbitals of TM to p_z orbitals of C and N of g-C_3N_4. As near the Fermi energy (E_F), the occupied energy states are mainly dominated by minority spin d-electrons and empty states arise from p_z of C and N atoms, transitions among them give the absorptions at low energy. Whereas, the absorption peaks, corresponding to the d–d transition of minority spin d-electrons appear at relatively higher energy window i.e. 2–3 eV. Now, d-orbitals of Cu- and Zn-g-C_3N_4 are completely filled and appear at ~1eV below the E_F. As a result, the transitions at <1eV energy range do not involve these d-orbitals of TM. Consequently, for these two sheets, absorption peaks at 0–1.0 eV appear from p_π→ p_π transitions of C and N of g-C_3N_4, whereas $d_{xy}/d_{x^2-y^2}$ → p_π and d_{zx}/d_{yz} /d_{z^2} → p_π (i.e. TM→ g-C_3N_4) transitions lead to absorptions at energy range of 1–2.5 eV and 2.5–3.5 eV, respectively. So, transitions at visible light energy range for all TM-g-C_3N_4, involve d-orbitals of TM which directly points towards the fact that the presence of TMs modify the photoabsorption property of these sheets.

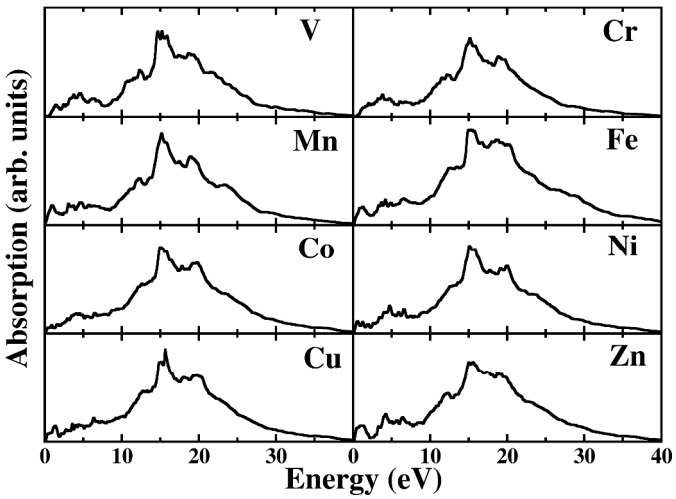

Figure 6. Computed absorption spectra of TM-g-C_3N_4 where TMs are written at the upper right corner of each plot. Red and black '*' denote the high intensity peaks at energy range of 0–2 and 2–3.5 eV, respectively. We have used a Gaussian broadening of 0.05 eV.

Conclusions

In conclusion, systematically preforming first-principles computation, we have demonstrated the structural, electronic, magnetic and optical properties of TM embedded g-C_3N_4 sheets. From our simulations it is evident that based on atomic radius of TMs, these sheets get geometrically modified from its bare buckled form to dissimilar other forms. Further, we have provided evidence for the regular ordering of single TM atoms on the cavity of g-C_3N_4 sheet by ruling out the possibility of

dimer or cluster formation of TM atoms. Performing AIMD, it becomes clear that these modifications occur in same way at finite temperature (300K) also. The thermal stability of these sheets are also confirmed by computing their structures at 500 K and 1000 K. Interestingly, transition metals which contain major part of magnetic moments of these sheets, magnetically couple in different ways and show wide-range of the magnetic ground states, from ferromagnetic to non-magnetic state. The origin of this magnetic interaction can be qualitatively inferred by Heitler and London model. The inclusion of metals converts the electrical nature of this sheet from wide gap semiconductor to metallic. Monte Carlo simulations based on Heisenberg model, show that ferromagnetic ordering of TMs e.g., V-, Cr- and Fe-g-C_3N_4, retain up to 205 K, 170.5 K and 115 K, respectively. Moreover, as the band-gap of g-C_3N_4 closes by TM inclusion, visible photoresponse also gets modify in large extent. The prominent absorption peaks at low energy range for these sheets confirms the ability to absorb visible light. Therefore, our study strongly demonstrates the possibility of multifunctional performance of these 2D-sheets. With progress of experimental techniques, we hope that these promising properties of the TM embedded g-C_3N_4 systems would be realized in near future.

Acknowledgements

DG acknowledges Dr. Suman Majumdar for fruitful discussions. GP acknowledges UGC-FRP for funding. BP acknowledges UGC Government of India, SKP acknowledges research support from the DST, Government of India.

Notes and references

[a] Chemistry and Physics of Materials Unit, Jawaharlal Nehru Centre for Advanced Scientific Research, Bangalore, 560064, India

[b] Department of Chemistry, Central College Campus, Bangalore University, Bangalore - 1.

[c] Theoretical Sciences Unit, Jawaharlal Nehru Centre for Advanced Scientific Research, Bangalore, 560064, India

† Electronic Supplementary Information (ESI) available: [Isosurface of charge density, PDOS, 2X2 supercell of g-C_3N_4 sheet, MD snapshots of sheets, spin density of sheets, details of magnetic coupling calculations]. See DOI: 10.1039/b000000x/

References

1 Y. Cui and C. M. Lieber, *Science*, 2001, **291**, 851-853.

2 T. Miyamachi, T. Schuh, T. Markl, C. Bresch, T. Balashov, A. Stohr, C. Karlewski, S. Andre, M. Marthaler, M. Hoffmann, M. Geilhufe, S. Ostanin, W. Hergert, I. Mertig, G. Schon, A. Ernst and W. Wulfhekel, *Nature*, 2013, **503**, 242-246.

3 M. Warner, S. Din, I. S. Tupitsyn, G. W. Morley, A. M. Stoneham, J. A. Gardener, Z. Wu, A. J. Fisher, S. Heutz, C. W. M. Kay and G. Aeppli, *Nature*, 2013, **503**, 504-508.

4 J. S. Miller and A. J. Epstein, *Angew. Chem. Int. Ed.*, 1994, **33**, 385-415.

5 A. R. Rocha, V. M. Garcia-Suarez, S. W. Bailey, C. J. Lambert, J. Ferrer and S. Sanvito, *Nature Mater.*, 2005, **4**, 335-339.

6 M. Ratner, *Nat Nano*, 2013, **8**, 378-381.

7 M. Jamet, W. Wernsdorfer, C. Thirion, D. Mailly, V. Dupuis, P. Mélinon and A. Pérez, *Phys. Rev. Lett.*, 2001, **86**, 4676-4679.

8 D. Kechrakos and K. N. Trohidou, *Physica B*, 2002, **318**, 360-364.

9 S. Moller, C. Perlov, W. Jackson, C. Taussig and S. R. Forrest, *Nature*, 2003, **426**, 166-169.

10 O. R. Nascimento, A. J. A. d. Oliveira, E. C. Pereira, A. A. Correa and L. Walmsley, *J. Phys.: Condens. Matter*, 2008, **20**, 035214.

11 L. Zhou, S.-W. Yang, M.-F. Ng, M. B. Sullivan, V. B. C. Tan and L. Shen, *J. Am. Chem. Soc.*, 2008, **130**, 4023-4027.

12 S. S. Mallajosyula and S. K. Pati, *J. Phys. Chem B*, 2008, **112**, 16982-16989.

13 D. Ghosh, P. Parida and S. K. Pati, *J. Phys. Chem C*, 2012, **116**, 18487-18494.

14 P. V. Radovanovic, C. J. Barrelet, S. Gradečak, F. Qian and C. M. Lieber, *Nano Lett.*, 2005, **5**, 1407-1411.

15 A. Bisig, M. Stärk, M.-A. Mawass, C. Moutafis, J. Rhensius, J. Heidler, F. Büttner, M. Noske, M. Weigand, S. Eisebitt, T. Tyliszczak, B. Van Waeyenberge, H. Stoll, G. Schütz and M. Kläui, *Nat Commun*, 2013, **4**.

16 S. K. Saha, M. Baskey and D. Majumdar, *Adv. Mater.*, 2010, **22**, 5531-5536.

17 Z. Zhang, X. Zou, V. H. Crespi and B. I. Yakobson, *ACS Nano*, 2013.

18 K. M. McCreary, A. G. Swartz, W. Han, J. Fabian and R. K. Kawakami, *Phys. Rev. Lett.*, 2012, **109**, 186604.

19 RadisavljevicB, RadenovicA, BrivioJ, GiacomettiV and KisA, *Nat Nano*, 2011, **6**, 147-150.

20 J. Zhou and Q. Sun, *J. Am. Chem. Soc.*, 2011, **133**, 15113-15119.

21 M. Kan, J. Zhou, Q. Sun, Y. Kawazoe and P. Jena, *J. Phys. Chem. Lett.*, 2013, **4**, 3382-3386.

22 K. F. Mak, C. Lee, J. Hone, J. Shan and T. F. Heinz, *Phys. Rev. Lett.*, 2010, **105**, 136805.

23 E. Kan, M. Li, S. Hu, C. Xiao, H. Xiang and K. Deng, *J. Phys. Chem. Lett.*, 2013, **4**, 1120-1125.

24 Z. Zhang, X. Liu, B. I. Yakobson and W. Guo, *J. Am. Chem. Soc.*, 2012, **134**, 19326-19329.

25 M. Xu, T. Liang, M. Shi and H. Chen, *Chem. Rev.*, 2013, **113**, 3766-3798.

26 J.-S. Lee, *Electronic Materials Letters*, 2011, **7**, 175-183.

27 A. Chung, J. Deen, J.-S. Lee and M. Meyyappan, *Nanotechnology*, 2010, **21**, 412001.

28 S. A. Wolf, D. D. Awschalom, R. A. Buhrman, J. M. Daughton, S. von Molnar, M. L. Roukes, A. Y. Chtchelkanova and D. M. Treger, *Science*, 2001, **294**, 1488-1495.

29 D. D. Awschalom and M. E. Flatte, *Nat Phys*, 2007, **3**, 153-159.

30 A. K. Geim and K. S. Novoselov, *Nat Mater*, 2007, **6**, 183-191.

31 K. S. Novoselov, A. K. Geim, S. V. Morozov, D. Jiang, Y. Zhang, S. V. Dubonos, I. V. Grigorieva and A. A. Firsov, *Science*, 2004, **306**, 666-669.

32 D. Pacile, J. C. Meyer, C. O. Girit and A. Zettl, *Appl. Phys. Lett.*, 2008, **92**, 133107-133103.

33 Y. Lin, T. V. Williams and J. W. Connell, *J. Phys. Chem. Lett.*, 2009, **1**, 277-283.
34 J. N. Coleman, M. Lotya, A. O'Neill, S. D. Bergin, P. J. King, U. Khan, K. Young, A. Gaucher, S. De, R. J. Smith and *et.al*, *Science*, 2011, **331**, 568-571.
35 H. Li, G. Lu, Z. Yin, Q. He, H. Li, Q. Zhang and H. Zhang, *Small*, 2012, **8**, 682-686.
36 Y. Omomo, T. Sasaki, Wang and M. Watanabe, *J. Am. Chem. Soc.*, 2003, **125**, 3568-3575.
37 X. Li, J. Zhou, Q. Wang, Y. Kawazoe and P. Jena, *J. Phys. Chem. Lett.*, 2012, **4**, 259-263.
38 Y. Zhang, T. Mori, L. Niu and J. Ye, *Energy Environ. Sci.*, 2011, **4**, 4517-4521.
39 Y. Zhang, T. Mori, J. Ye and M. Antonietti, *J. Am. Chem. Soc.*, 2010, **132**, 6294-6295.
40 A. Thomas, A. Fischer, F. Goettmann, M. Antonietti, J.-O. Muller, R. Schlogl and J. M. Carlsson, *J. Mater. Chem.*, 2008, **18**, 4893-4908.
41 A. V. Krasheninnikov, P. O. Lehtinen, A. S. Foster, P. Pyykko and R. M. Nieminen, *Phys. Rev. Lett.*, 2009, **102**, 126807.
42 M. Chen, Y.-J. Zhao, J.-H. Liao and X.-B. Yang, *Phys. Rev. B*, 2012, **86**, 45459.
43 T. P. Hardcastle, C. R. Seabourne, R. Zan, R. M. D. Brydson, U. Bangert, Q. M. Ramasse, K. S. Novoselov and A. J. Scott, *Phys. Rev. B*, 2013, **87**, 195430.
44 O. Cretu, A. V. Krasheninnikov, J. A. Rodríguez-Manzo, L. Sun, R. M. Nieminen and F. Banhart, *Phys. Rev. Lett.*, 2010, **105**, 196102.
45 B. Huang, H. Xiang, J. Yu and S.-H. Wei, *Phys. Rev. Lett.*, 2012, **108**, 206802.
46 Y. Lu, X. Zuo, M. Feng and T. Zhou, *J. Appl. Phys.*, 2013, **113**, -.
47 A. W. Robertson, B. Montanari, K. He, J. Kim, C. S. Allen, Y. A. Wu, J. Olivier, J. Neethling, N. Harrison, A. I. Kirkland and *et.al.*, *Nano Lett.*, 2013, **13**, 1468–1475.
48 X. Ma, Y. Lv, J. Xu, Y. Liu, R. Zhang and Y. Zhu, *J. Phys. Chem C*, 2012, **116**, 23485-23493.
49 X. Chen, J. Zhang, X. Fu, M. Antonietti and X. Wang, *J. Am. Chem. Soc.*, 2009, **131**, 11658-11659.
50 E. Z. Lee, Y.-S. Jun, W. H. Hong, A. Thomas and M. M. Jin, *Angew. Chem. Int. Ed.*, 2010, **49**, 9706-9710.
51 X. Wang, X. Chen, A. Thomas, X. Fu and M. Antonietti, *Adv. Mater.*, 2009, **21**, 1609-1612.
52 G. Ding, W. Wang, T. Jiang, B. Han, H. Fan and G. Yang, *ChemCatChem*, 2013, **5**, 192-200.
53 J. Tian, Q. Liu, A. M. Asiri, A. O. Al-Youbi and X. Sun, *Anal. Chem.*, 2013, **85**, 5595-5599.
54 P. Niu, L. Zhang, G. Liu and H.-M. Cheng, *Adv. Funct. Mater.*, 2012, **22**, 4763-4770.
55 M. Deifallah, P. F. McMillan and F. Cora, *J. Phys. Chem C*, 2008, **112**, 5447-5453.
56 X. Wang, K. Maeda, A. Thomas, K. Takanabe, G. Xin, J. M. Carlsson, K. Domen and M. Antonietti, *Nat Mater*, 2009, **8**, 76-80.
57 G. Algara-Siller, N. Severin, S. Y. Chong, T. Björkman, R. G. Palgrave, A. Laybourn, M. Antonietti, Y. Z. Khimyak, A. V. Krasheninnikov, J. P. Rabe, U. Kaiser, A. I. Cooper, A. Thomas and M. J. Bojdys, *Angew. Chem. Int. Ed.*, 2014.
58 X. Zhang, X. Xie, H. Wang, J. Zhang, B. Pan and Y. Xie, *J. Am. Chem. Soc.*, 2012, **135**, 18-21.
59 S. Yang, Y. Gong, J. Zhang, L. Zhan, L. Ma, Z. Fang, R. Vajtai, X. Wang and P. M. Ajayan, *Adv. Mater.*, 2013, **25**, 2452-2456.
60 L. Sorace, C. Benelli and D. Gatteschi, *Chem. Soc. Rev.*, 2011, **40**, 3092-3104.
61 J. Zhang, J. Sun, K. Maeda, K. Domen, P. Liu, M. Antonietti, X. Fu and X. Wang, *Energy Environ. Sci.*, 2011, **4**, 675-678.
62 G. Kresse and J. Furthmüller, *Phys. Rev. B*, 1996, **54**, 11169-11186.
63 J. P. Perdew, K. Burke and M. Ernzerhof, *Phys. Rev. Lett.*, 1996, **77**, 3865-3868.
64 I. A. Vladimir, F. Aryasetiawan and A. I. Lichtenstein, *J. Phys.: Condens. Matter*, 1997, **9**, 767.
65 K. Sato, L. Bergqvist, J. Kudrnovský, P. H. Dederichs, O. Eriksson, I. Turek, B. Sanyal, G. Bouzerar, H. Katayama-Yoshida, V. A. Dinh and *et.al.*, *Rev. Mod. Phys.*, 2010, **82**, 1633-1690.
66 M. Bernien, J. Miguel, C. Weis, M. E. Ali, J. Kurde, B. Krumme, P. M. Panchmatia, B. Sanyal, M. Piantek, P. Srivastava and *et.al.*, *Phys. Rev. Lett.*, 2009, **102**, 047202.
67 G. Kresse and D. Joubert, *Phys. Rev. B*, 1999, **59**, 1758-1775.
68 P. E. Blöchl, *Phys. Rev. B*, 1994, **50**, 17953-17979.
69 S. H. Vosko, L. Wilk and M. Nusair, *Can. J. Phys.*, 1980, **58**, 1200-1211.
70 S. Nose, *J. Chem. Phys.*, 1984, **81**, 511-519.
71 W. G. Hoover, *Phys. Rev. A*, 1985, **31**, 1695-1697.
72 Y. Tang, Z. Yang and X. Dai, *J. Chem. Phys.*, 2011, **135**, -.
73 J. Heyd, G. E. Scuseria and M. Ernzerhof, *J. Chem. Phys.*, 2006, **124**, -.
74 R. Zan, U. Bangert, Q. Ramasse and K. S. Novoselov, *Nano Lett.*, 2011, **11**, 1087-1092.
75 M. Chen, Y.-J. Zhao, J.-H. Liao and X.-B. Yang, *Phys. Rev. B*, 2012, **86**, 045459.
76 M. Chen, X.-B. Yang, J. Cui, J.-J. Tang, L.-Y. Gan, M. Zhu and Y.-J. Zhao, *Int. J. Hydrogen Energy*, 2012, **37**, 309-317.
77 R. Shannon, *Acta Crystallographica Section A*, 1976, **32**, 751-767.
78 A. Fasolino, J. H. Los and M. I. Katsnelson, *Nat Mater*, 2007, **6**, 858-861.
79 K. O., *Molecular Magnetism* VCH, New York, 1993.
80 S. S. Mallajosyula and S. K. Pati, *Angew. Chem. Int. Ed.*, 2009, **48**, 4977-4981.
81 J. He, S. Y. Ma, P. Zhou, C. X. Zhang, C. He and L. Z. Sun, *J. Phys. Chem C*, 2012, **116**, 26313-26321.
82 J. He, N. Jiao, C. Zhang, H. Xiao, X. Chen and L. Sun, *J. Phys. Chem C*, 2014, **118**, 8899-8906.
83 D. Landau, Binder Kurt, *A Guide to Monte Carlo Simulations in Statistical Physics*, Cambridge, 2000.